

Contents lists available at ScienceDirect

International Journal of Refractory Metals and Hard Materials

journal homepage: www.elsevier.com/locate/IJRMHM



Microstructure, mechanical properties and tribocorrosion characteristics of $(Mo_{1-x}Cr_x)_5Si_3$ alloys

R.P. Li, H. Chen*, X.H. Hao, X.C. Zhao, B.X. Huang

School of Materials Science and Engineering, Liaocheng University, Liaocheng, Shandong 252000, China

ARTICLE INFO

$\it Keywords$: $\it Mo_5Si_3$ $\it Microstructure$ $\it Mechanical properties$ $\it Tribocorrosion behavior$ $\it Combined effect$

ABSTRACT

 $(Mo_{1-x}Cr_x)_5Si_3$ alloys were prepared by vacuum arc melting technique. The microstructure and mechanical properties of $(Mo_{1-x}Cr_x)_5Si_3$ alloys were characterized using a scanning electron microscope (SEM), X-ray diffraction (XRD) and nano-indentation tests. The tribocorrosion characteristics of the alloys were investigated using a tribocorrosion tester in 3.5 wt% NaCl solution. The results revealed that the thermal expansion anisotropy ((CTE(c)/CTE(a))) of the $(Mo_{1-x}Cr_x)_5Si_3$ alloys decreased from 2.25 to 1.45 with increasing Cr content. The Cr-alloyed $(Mo_{1-x}Cr_x)_5Si_3$ alloys exhibited a high hardness, and their fracture toughness, ratios of H^3/E^2 and H/E were improved. $(Mo_{1-x}Cr_x)_5Si_3$ alloys showed a strong wear-corrosion combined effect, and an opposite trend between friction coefficient and OCP values was observed during the tribocorrosion tests. The tribocorrosion resistances of $(Mo_{1-x}Cr_x)_5Si_3$ alloys were better than that of 0Cr18Ni9 stainless steel due to the formation of Cr_2O_3 - MoO_3 - SiO_x protective films. The $(Mo_{0.8}Cr_{0.2})_5Si_3$ alloy exhibited the best tribocorrosion characteristics with a low friction coefficient and wear rate. For the 0Cr18Ni9 and Mo_5Si_3 alloy, pure wear (V_w) was dominant, nevertheless, corrosion-induced wear (V_{cw}) was the main tribocorrosion mechanism of $(Mo_{0.8}Cr_{0.2})_5Si_3$ alloy.

1. Introduction

Wear and corrosion are the two major modes of material failure [1,2]. The combined effect of wear and corrosion processes is defined as tribocorrosion [3,4]. In many cases, wear is accelerated by corrosion, and similarly, corrosion can be accelerated by the wear process [5]. Their interaction or combined effect usually leads to a decrease in material performance and accelerated material failure [6,7]. This material removal due to tribocorrosion cannot be measured by a simple sum of separate wear and corrosion experiments [8]. As the traditional corrosion-resistant materials, austenitic stainless steels exhibit good resistance against most corrosive media. However, their mechanical moving contact components tend to fail prematurely in corrosive environments due to their low hardness and poor wear resistance [9,10]. On the other hand, conventional wear-resistant materials such as white cast iron, high-carbon steel, and alloy tool steels are difficult to be applied in tribocorrosion conditions due to insufficient corrosion resistance [11]. As an important branch of intermetallic compounds, the metal silicides (such as Mo-Si [12], Ti-Si [13], Cr-Si [14], and Ni-Si [15] binary compounds and their multi-component alloys) demonstrate excellent hardness, high-temperature strength and chemical stability, and shows a

great potential to be used as anti-corrosion and wear-resistant materials in engineering applications [16]. However, their serious room temperature brittleness is a major obstacle to engineering applications.

Used to replace Ni-based superalloys and some functional materials, Mo-Si alloys have recently attracted great interest in advanced jet engine blades and automotive applications, energy storage, and thermoelectric devices due to their high melting point, moderate density and high creep resistance [17,18]. In particular, Mo₅Si₃ has a relatively wide range of chemical components according to the Mo-Si binary phase diagram, which provides the possibility of improving its properties by introducing different alloying elements [19]. Recent studies [20-22] have demonstrated that alloying elements such as Cr, Ti, Ni and Al can effectively enhance the room temperature toughness and oxidation resistance of intermetallic compounds by modifying the crystal structure symmetry, lattice thermal expansion anisotropy and adjusting the percentage of metallic bonds in the alloys [23,24]. Additionally, the alloying of Ni promoted static and dynamic recrystallization of the alloy, which was beneficial for improving the deformation processing and intrinsic brittleness of the intermetallic compound [25]. Therefore, an alloyed Mo₅Si₃ intermetallic with a certain degree of toughening can be obtained by arc melting and containing different alloying elements.

E-mail address: chenhui002@qq.com (H. Chen).

 $^{^{\}ast}$ Corresponding author.

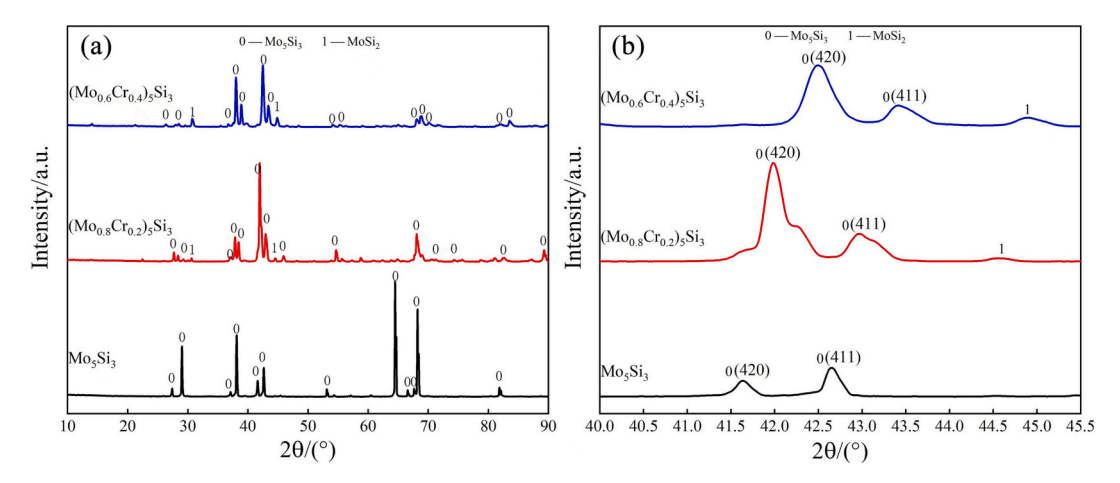
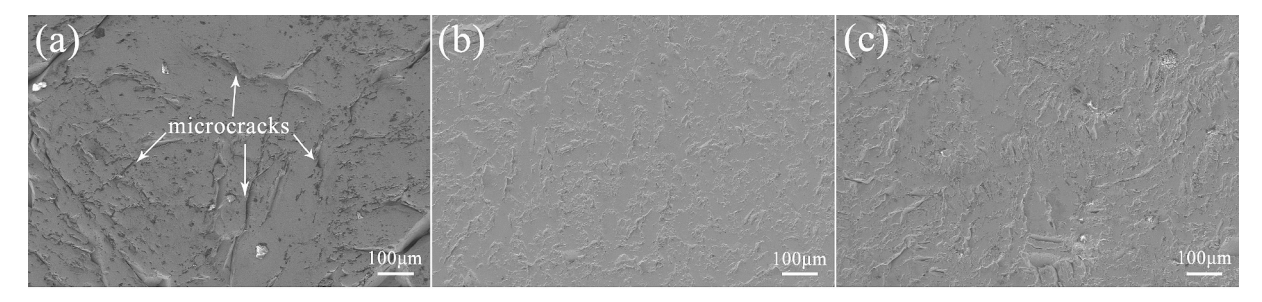


Fig. 1. (a) XRD patterns of the $(Mo_{1-x}Cr_x)_5Si_3$ alloys and (b) the stronger diffraction peaks of (420) and (411).



 $\textbf{Fig. 2.} \ \ \text{SEM images of } (\text{Mo}_{1\text{-}x}\text{Cr}_x)_5\text{S}i_3 \ \ \text{alloys. (a)} \ \ \text{Mo}_5\text{S}i_3 \text{, (b)} \ \ (\text{Mo}_{0.8}\text{Cr}_{0.2})_5\text{S}i_3 \text{, (c)} \ \ (\text{Mo}_{0.6}\text{Cr}_{0.4})_5\text{S}i_3 \text{.}$

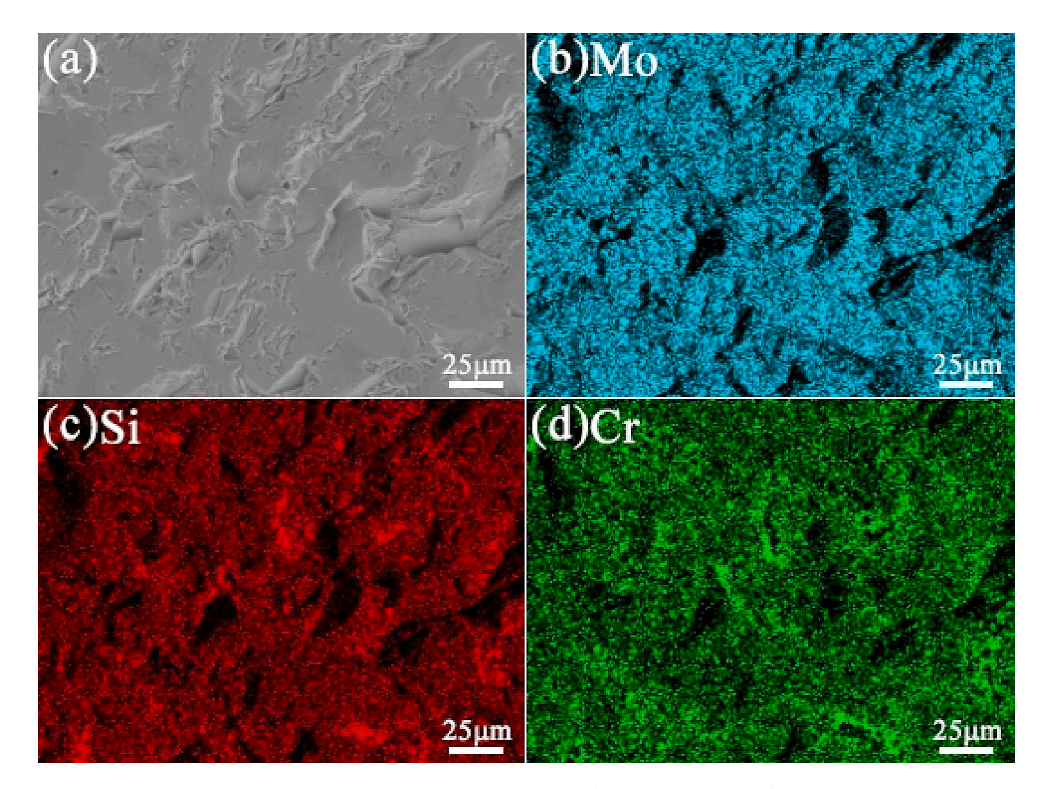


Fig. 3. The EDS elemental mapping of the $(Mo_{0.6}Cr_{0.4})_5Si_3$ alloy.

As a structural material application, the wear and corrosion resistance of the Mo_5Si_3 intermetallic alloy should be the most important factors to be considered. Wang et al. [26] reported that the good

corrosion resistance of silicide was closely related to the stronger Si—O bonds by first-principles calculations based on density functional theory (DFT). They concluded that Mo_5Si_3 should have excellent corrosion

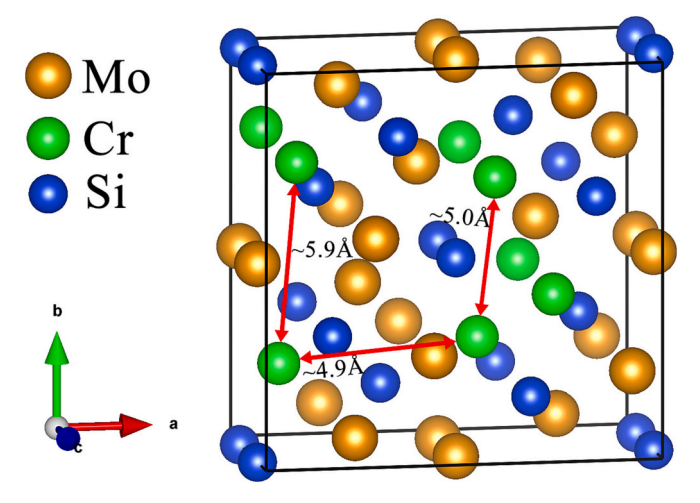


Fig. 4. Atomic structure of the (Mo, Cr)₅Si₃ cell containing eight Cr atoms.

resistance. Chen et al. [27] demonstrated that the Nb-alloyed Mo₅Si₃ alloys exhibit excellent corrosion resistance in 1 mol/L HCl and H2SO4 solutions. Jiang and Li et al. [28,29] investigated the effect of Cr and Al alloying on the corrosion and wear properties of Mo-Si alloys. The results indicated that the alloys can form more protective Cr2O3 and Al₂O₃ passivation films in NaCl solution by introducing a certain amount of Cr and Al elements. Moreover, the introduction of Cr and Al elements can refine the microstructure and strengthen the Mo-Mo and Mo-Si bonds, which improves the wear resistance of Mo₅Si₃ alloy. This indicates that the alloying elements have a significant impact on the corrosion and wear resistance of Mo₅Si₃ alloy. However, researches on the tribocorrosion characteristics of Mo₅Si₃-based alloys are still scarce. In the present study, (Mo_{1-x}Cr_x)₅Si₃ alloys with different Cr contents were prepared by arc melting. The microstructure, mechanical properties and tribocorrosion characteristics of the alloys were investigated in 3.5 wt% NaCl solution. The tribocorrosion mechanisms of (Mo_{1-x}Cr_x)₅Si₃ alloys were also discussed. The study of tribocorrosion-resistant (Mo₁₋ xCrx)5Si3 alloys will broaden the tribological application of Mo5Si3 intermetallic as structural materials under severe conditions.

2. Experiment details

2.1. Materials preparation and microstructure characterization

 $(Mo_{1-x}Cr_x)_5Si_3(x=0,\,0.2,\,0.4)$ alloys were prepared by arc melting using the high-purity Mo, Cr and Si powders (purity >99.5 wt%) as raw materials (raw powders were supplied by Sinopharm Chemical Reagent Co. Ltd., China). The initial powders were mixed and compacted into cylinders and then placed in a water-cooled copper crucible with a magnetic stirring device for arc melting. All ingots were re-melted at least five times in an Ar atmosphere (5 \times 10 4 Pa pressure) to ensure uniform distribution of the constituents. The ingots were flipped over for each remelt. Finally, Electric Discharge Machining (EDM, DK7740-B, Wuhan Xin Dexing CNC Machine Tools Co. Ltd., China) wire cutter was used to cut the ingots into 10 mm \times 10 mm \times 5 mm specimens for microstructure, mechanical properties and tribocorrosion behaviors

analysis.

Metallographic specimens of $(Mo_{1-x}Cr_x)_5Si_3$ alloys were prepared using mechanical grinding with waterproof abrasive sandpaper (from 400 to 1500 grit) and polished with diamond particle paste. The microstructures of the alloys were examined by optical microscopy (OM, Axio Scope A1, Germany) and scanning electron microscopy (SEM, Merlin Compact, ZEISS, Germany) and equipped with energy dispersive spectroscopy (EDS, JEOL, Japan) for elemental analysis. The phase structures of alloys were determined by X-ray diffraction (XRD, D/Dmax-2400, Rigaku, Japan) with Cu K α radiation (λ = 0.15418 nm) and a 2 θ range from 20° to 90°.

2.2. Mechanical properties of the $(Mo_{1-r}Cr_r)_5Si_3$ alloys

The microhardness of the $(Mo_{1-x}Cr_x)_5Si_3$ alloys was measured using an HVS-1000 hardness tester under an applied load of 500 g with a dwell time of 15 s. The average of at least five measurements was recorded as the hardness value. The fracture toughness values of the alloys were detected by the Vickers microhardness indentation test, and the lengths of the indentation cracks were measured using an optical microscope. Fracture toughness is calculated using the formula [30].

$$K_{IC} = 0.032 H_{\nu} a^{\frac{1}{2}} \left(\frac{E}{H_{\nu}}\right)^{\frac{1}{2}} \left(\frac{a}{c}\right)^{\frac{3}{2}} \tag{1}$$

where K_{IC} is the fracture toughness (MPa·m^{1/2}), E is the elastic modulus (MPa), H_{v} is the hardness (MPa), a and c are the indentation and radial crack lengths (m), respectively.

The nanoindentation hardness (*H*) and elastic modulus (*E*) of the alloys were measured using a Nano Indenter G200 (KLA-Tencor Co. Ltd., USA) equipped with a Berkovich diamond tip. Based on Oliver-Pharr [31], the tests were performed by driving the indenter at a constant loading rate of 40 mN/min under a peak load of 20 mN. For each alloy, nanoindentation tests were conducted at five different locations to ensure the repeatability of the experimental data.

2.3. Tribocorrosion properties of $(Mo_{1-x}Cr_x)_5Si_3$ alloys

To determine the tribocorrosion characteristics and the combined effect of wear and corrosion on material loss, the following three sets of experiments were performed. (1) The pure corrosion behavior of the alloys (no wear) was evaluated by measuring anodic polarization curves in 3.5 wt% NaCl solution using electrochemical test equipment (PGSTAT302N, Switzerland). High purity platinum was used as the counter electrode, the alloys are used as the working electrode (1 cm² exposure area) and a saturated calomel electrode (SCE) is used as the reference electrode. The potentials were swept from -0.5 V to +2 V (vs. reference electrode) at a sweep rate of 5 mV/s. (2) Tribocorrosion tests were performed using a three-electrode reciprocating tribocorrosion tester (MFT-R4000, China) in a 3.5 wt% NaCl solution. The Al₂O₃ ball with a diameter of 6 mm was selected as the counterpart for the tribocorrosion tests due to its high hardness and good corrosion resistance. High purity graphite was used as the counter electrode, the alloys as the working electrode (1 cm² exposure area), and a saturated calomel electrode as the reference electrode. The OCP and friction coefficient were first recorded for 600 s to ensure a stable electrochemical state of

Table 1 Lattice parameters, crystallite size, microstrain and CTE of the $(Mo_{1-x}Cr_x)_5Si_3$ alloys.

Compound	Lattice parameters			Crystallite size (nm)	Microstrain (%)	CTE (c)/CTE (a)
	a (Å)	c (Å)	V _c (Å ³)			
Mo ₅ Si ₃ (JCPDS, 65–2783)	9.620	4.900	453.5	_	_	_
Mo ₅ Si ₃	9.625	4.894	453.4	83.1	0.299	2.21
$(Mo_{0.8}Cr_{0.2})_5Si_3$	9.574	4.868	446.2	65.0	0.661	1.63
$(Mo_{0.6}Cr_{0.4})_5Si_3$	9.537	4.852	441.3	45.9	0.731	1.45

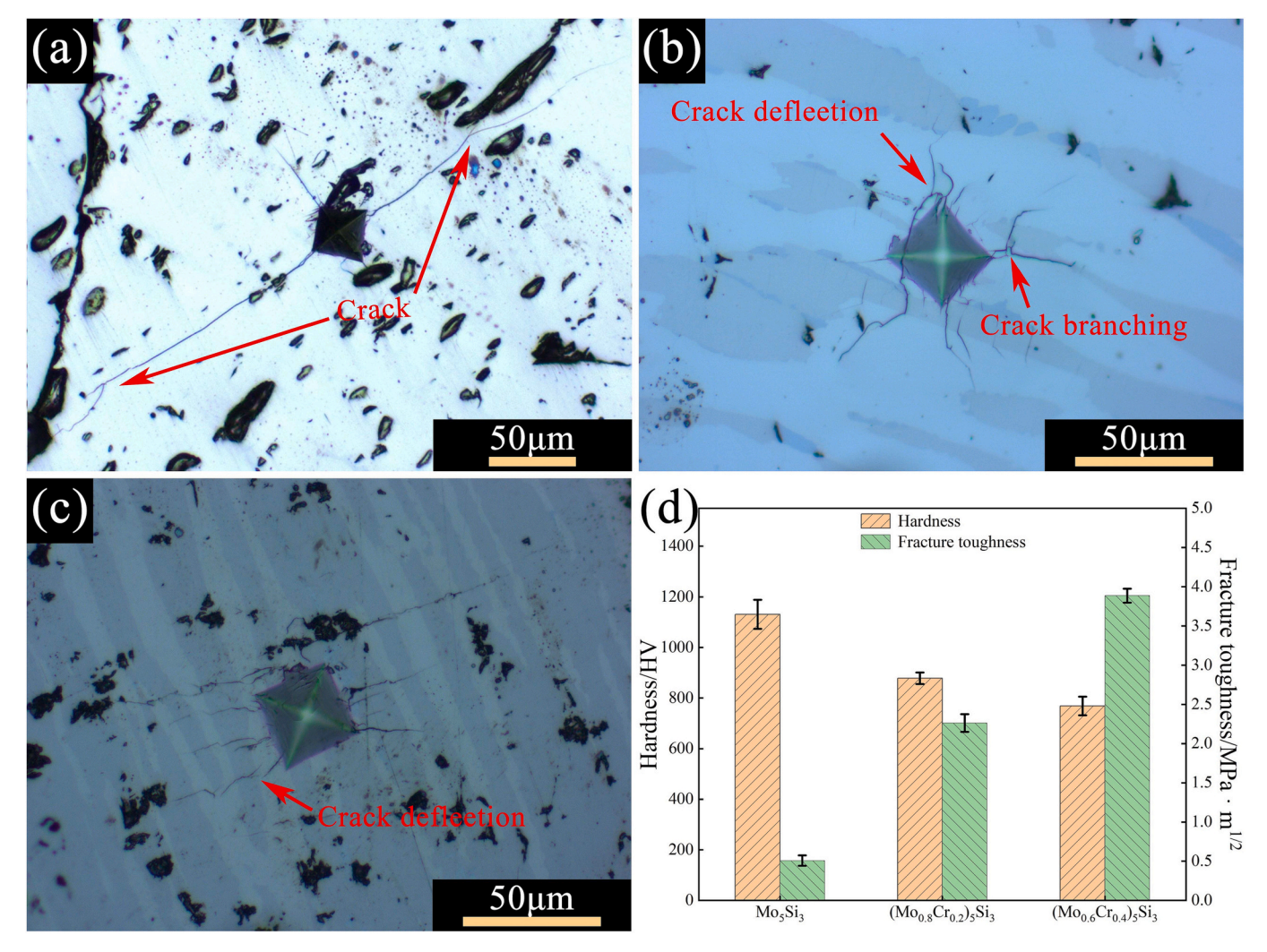


Fig. 5. Typical hardness indentation image (a-c), microhardness and fracture toughness (d) of $(Mo_{1-x}Cr_x)_5Si_3$ alloys. (a) Mo_5Si_3 , (b) $(Mo_{0.8}Cr_{0.2})_5Si_3$ and (c) $(Mo_{0.6}Cr_{0.4})_5Si_3$.

the alloy surface prior to the tribocorrosion test under open-circuit potential conditions. During the tribocorrosion test, the reciprocating sliding test was performed with a normal load of 5 N, a sliding amplitude of 5 mm, a frequency of 2 Hz, and a sliding time of 2400 s. When the sliding wear stopped, the OCP and friction coefficient were continuously recorded for 600 s to evaluate the passivation behaviors of the (Mo₁. _xCr_x)₅Si₃ alloys surface. (3) In order to calculate the material loss caused by pure wear behavior under the same condition as above, simple pure wear tests were conducted in deionized water. All tests were repeated three times to check the reproducibility of the experimental results. The surface state of the tribocorrosion tracks was observed and analyzed by SEM, EDS, and X-ray photoelectron spectroscopy (XPS). For the XPS test, a Kratos AXIS Ultra ESCA system with Al Ka (1486.6 eV) was selected as the X-ray source. The accelerating voltage, emission current, and electron emission angle of the X-ray source were kept at 12 kV, 12 mA, and 45°, respectively. The conventional corrosion-resistant material 304 stainless steel (0Cr18Ni9) was used as a reference material and its tribocorrosion characteristics were tested under the same conditions.

3. Results and discussion

3.1. Microstructures and phase analysis

Fig. 1 shows the X-ray diffraction patterns of the $(Mo_{1-x}Cr_x)_5Si_3$ (x = 0, 0.2, 0.4) alloys. As can be clearly seen, all melted alloys consist of a

hexagonal D8m-structured Mo_5Si_3 (JCPDS, 65–2783) and a small amount of hexagonal C40-structured $MoSi_2$ (JCPDS, 65–9392). The diffraction peak intensity of $MoSi_2$ in the alloy increases with the increase of Cr content, which is attributed to the destruction of the structural stability and orderliness of Mo_5Si_3 by the addition of Cr [19]. With increasing Cr content, the diffraction peak position shifts to higher 2θ values than that of the pure Mo_5Si_3 (in Fig. 1(b)), indicating that the solid solution of Cr into Mo_5Si_3 reduces the lattice parameters and interplanar spacing due to the smaller atomic radius of Cr compared to Mo_3Si_3 and Mo_3Si_3 reduces the lattice parameters and interplanar spacing due to the smaller atomic radius of Cr compared to Mo_3Si_3 reduces the lattice parameters and interplanar spacing due to the smaller atomic radius of Cr compared to Mo_3Si_3 reduces the lattice parameters and interplanar spacing due to the smaller atomic radius of Cr compared to Mo_3Si_3 reduces the lattice parameters and interplanar spacing due to the smaller atomic radius of Cr compared to Mo_3Si_3 reduces the lattice parameters and interplanar spacing due to the smaller atomic radius of Cr compared to Mo_3Si_3 reduces the lattice parameters and Mo_3Si_3 re

Fig. 2 shows the typical SEM micrographs of the $(Mo_{1-x}Cr_x)_5Si_3$ (x = 0, 0.2, 0.4) alloys. In Fig. 2 (a), some microcracks were observed due to high thermal stresses incurred during arc melting. In contrast, the $(Mo_{0.8}Cr_{0.2})_5Si_3$ alloy exhibited a uniformly dense and refined microstructure (Fig. 2 (b)), indicating that the Cr alloying contributed to the reduction of internal stresses and refinement of the matrix structure. Nonetheless, as the Cr content increased, $MoSi_2$ and Cr-rich phases were formed in the $(Mo_{0.6}Cr_{0.4})_5Si_3$ alloy, which increased the surface defects due to residual strain caused by the differences in elastic modulus and/or thermal expansion mismatch between the different phases, as shown in Fig. 2 (c) and the EDS elemental mapping of the $(Mo_{0.6}Cr_{0.4})_5Si_3$ alloy in Fig. 3.

It is generally accepted that high internal stress not only affects the surface state of the alloy but also has a great influence on the mechanical properties, corrosion and wear properties of the materials [23].

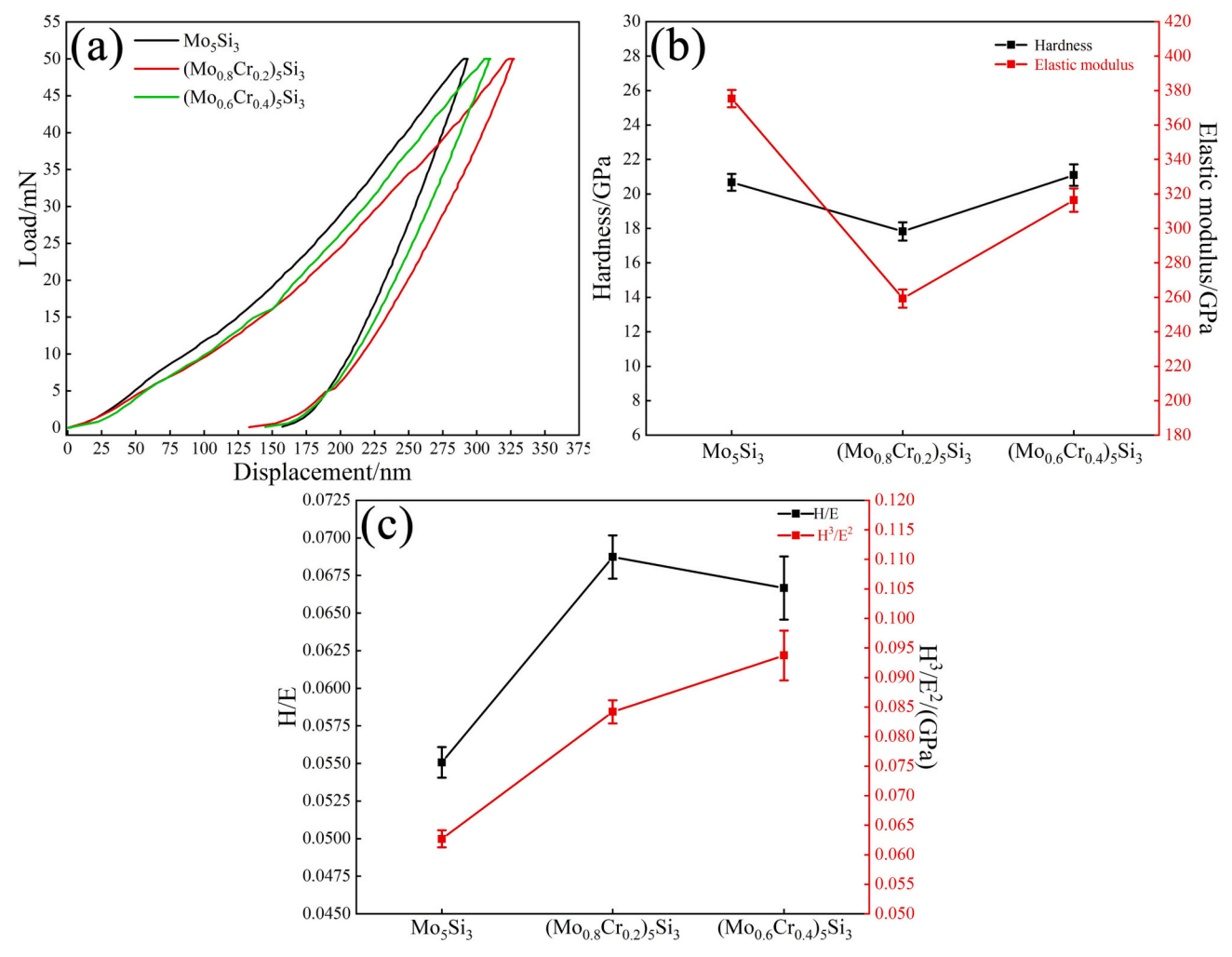
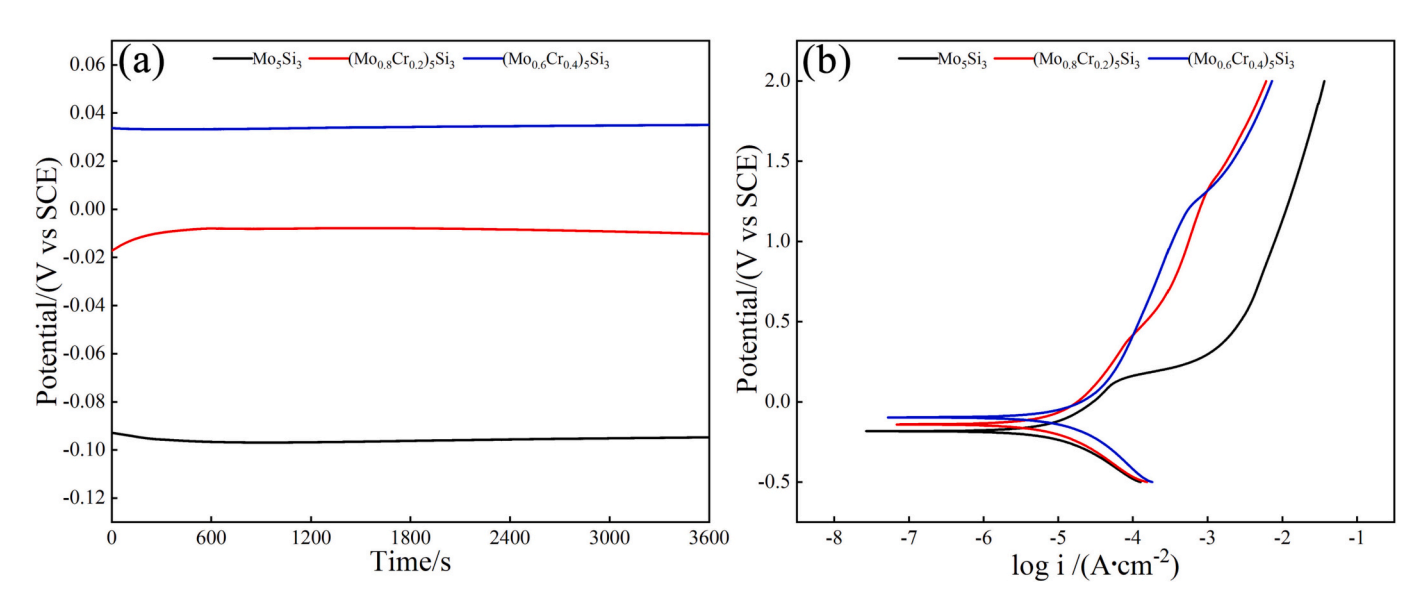


Fig. 6. Load-displacement curves (a), hardness and elastic modulus (b), and H/E and H^3/E^2 (c) of $(Mo_{1-x}Cr_x)_5Si_3$ alloys.



 $\textbf{Fig. 7.} \ \ \text{Open circuit potential (a) and potentiodynamic polarization curves (b) of } \\ (\text{Mo}_{1-x}\text{Cr}_x)_5\text{Si}_3 \ \text{alloys in 3.5 wt\% NaCl solution.} \\$

Unfortunately, the transition metal silicides Mo_5Si_3 exhibit a large difference in the coefficients of thermal expansion (CTE) in the a and c crystallographic directions, resulting in a high thermal expansion

anisotropy. Knowing the crystal structure of Mo_5Si_3 is a prerequisite for understanding thermal expansion anisotropy. Mo_5Si_3 belongs to the I4/mcm space group and has 20 Mo atoms and 12 Si atoms in the body-

 $\begin{tabular}{ll} \textbf{Table 2} \\ \textbf{The electrochemical parameters obtained from the polarization curves in 3.5 wt} \\ \textbf{\% NaCl solution.} \\ \end{tabular}$

Samples	E _{corr} (V vs SCE)	i _{corr} (μA/cm ²)	E _b (V vs SCE)
Mo ₅ Si ₃	-0.183	26.07	0.123
$(Mo_{0.8}Cr_{0.2})_5Si_3$	-0.141	21.85	0.383
$(Mo_{0.6}Cr_{0.4})_5Si_3$	-0.097	32.11	1.215

centered tetragonal (tl32) unit cell. Its lattice parameter a is twice as large as c, as shown in Fig. 4. It has been shown that the introduction of alloying elements such as Cr, Ti and Nb into Mo_5Si_3 can effectively adjust the lattice parameters and reduce the thermal expansion anisotropy [32]. Table 1 shows the effect of Cr alloying on the lattice parameters, grain size, microstrain and CTE of Mo_5Si_3 . Significantly, Cr alloying reduces the lattice parameters and grain size of the $(Mo_1 \ _xCr_x)_5Si_3$ alloys. The coefficients of thermal expansion of the $(Mo_1 \ _xCr_x)_5Si_3$ alloys were calculated using eq. (2) [23]

$$CTE = \begin{pmatrix} 1/l_0 \end{pmatrix} \cdot \begin{pmatrix} dl/dT \end{pmatrix}$$
 (2)

where l_0 is the lattice parameter at 293 K and dl/dT is the derivative of the lattice parameter with respect to temperature variation. The lattice parameter data of $(Mo_{1-x}Cr_x)_5Si_3$ alloys at different temperatures were obtained from Table 1 and first-principles theoretical calculations [19]. The calculations were based on the density functional theory using a plane-wave pseudo-potential method. It can be seen that the limited solid solution of Cr in Mo_5Si_3 can decrease the mismatch of CTE values in the a and c directions. The ratio of CTE (c)/CTE (a) decreases from 2.21 to 1.45 with the increase of Cr content, which is helpful in reducing the internal stress and improving the fracture toughness of $(Mo_{1-x}Cr_x)_5Si_3$ alloys.

3.2. Mechanical properties of $(Mo_{1-x}Cr_x)_5Si_3$ alloys

A typical hardness indentation image, hardness and fracture toughness of the $(Mo_{1\text{-}x}Cr_x)_5Si_3$ alloys are shown in Fig. 5. In Fig. 5 (a), apparent microcracks were detected at the ends and edges of the

diamond-shaped indentations due to the high intrinsic brittleness. In Fig. 5 (b, c), the Cr alloying refined the matrix crystallites and increased the grain boundaries, thus raising the fracture energy required for the material. Additionally, due to the Cr alloying and the formation of the MoSi₂ phase, the cracks in the Mo₅Si₃ matrix are deflected, branched and bridged (Fig. 5 (b, c)). This causes the crack propagation to become tortuous, reduces the stress at the crack front, consumes the crack propagation energy, and improves the fracture toughness of the (Mo₁. _xCr_x)₅Si₃ alloys, as shown in Fig. 5 (d). Furthermore, in contrast to conventional solid solution strengthening, the microhardness of the (Mo_{1-x}Cr_x)₅Si₃ alloys was decreased with increasing Cr content (in Fig. 5 (d)). Solid solution softening or strengthening of the material by alloying is commonly attributed to variations in Peierls potentials and dislocation core structures [28]. Thus, solid solution softening of the Mo₅Si₃ alloy occurs through Cr alloying due to reduced stacking fault energy and Peierls stress [33].

Fig. 6 (a) shows typical load-displacement curves for (Mo_{1-x}Cr_x)₅Si₃ alloys. The load-displacement curve has no significant protrusions. indicating that the loads cause only elastic-plastic deformation of the alloy surface. The closed area surrounded by the loading-unloading curve and the largest displacement of the Mo₅Si₃ alloy is smaller than that of the (Mo_{0.8}Cr_{0.2})₅Si₃ and (Mo_{0.6}Cr_{0.4})₅Si₃ alloys. This indicates that the plastic deformation capacity of Cr alloyed Mo₅Si₃ was improved during loading. The (Mo_{0.8}Cr_{0.2})₅Si₃ alloy exhibited the largest plastic deformation as well as lower hardness and elastic modulus. In general, a large H³/E² ratio indicates a high plastic deformation resistance and correspondingly improved toughness [34]. As seen in Fig. 6 (c), the H³/ E² values of the alloys increase with an increase in Cr content. Among the alloys, the $(Mo_{0.6}Cr_{0.4})_5Si_3$ alloy exhibits the highest H^3/E^2 values and good toughness. This demonstrated that the Cr alloying has a toughening effect on the Mo₅Si₃ alloy, which is consistent with the results in Fig. 5 (d). High toughness is crucial for eliminating fatigue and wear damage during sliding. On the other hand, the H/E ratio as a mechanical parameter is considered useful for predicting the wear resistance of a material [25]. Based on this criterion, (Mo_{0.8}Cr_{0.2})₅Si₃ alloy has a high H/E ratio and should have better wear resistance than other alloys.

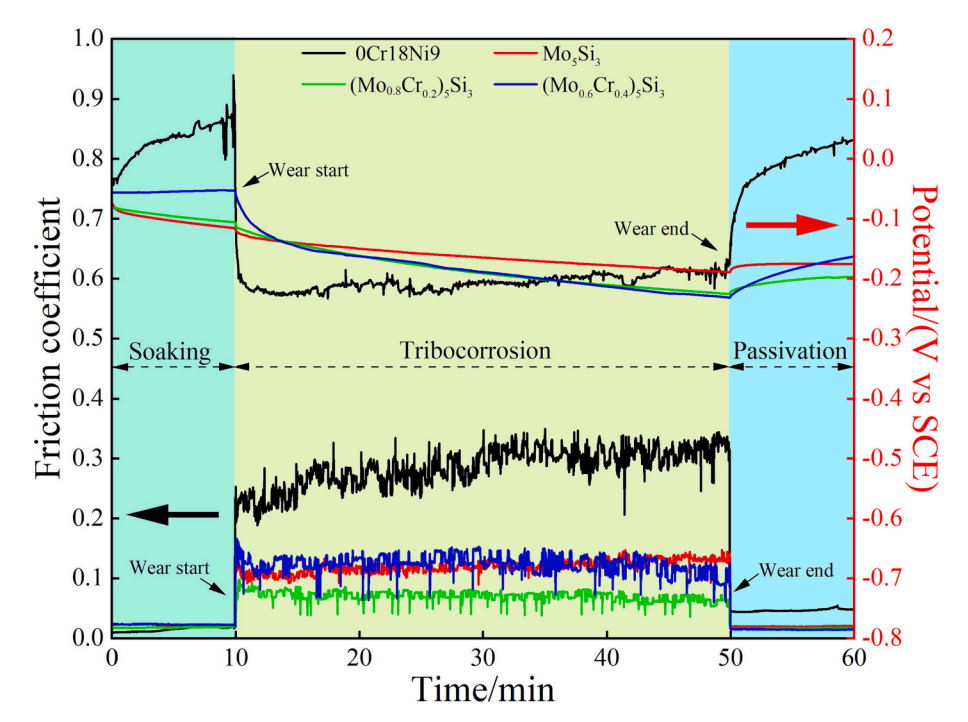


Fig. 8. Variation of friction coefficient curves and corresponding OCP of (Mo_{1-x}Cr_x)₅Si₃ alloys sliding against Al₂O₃ balls in 3.5 wt% NaCl solution.

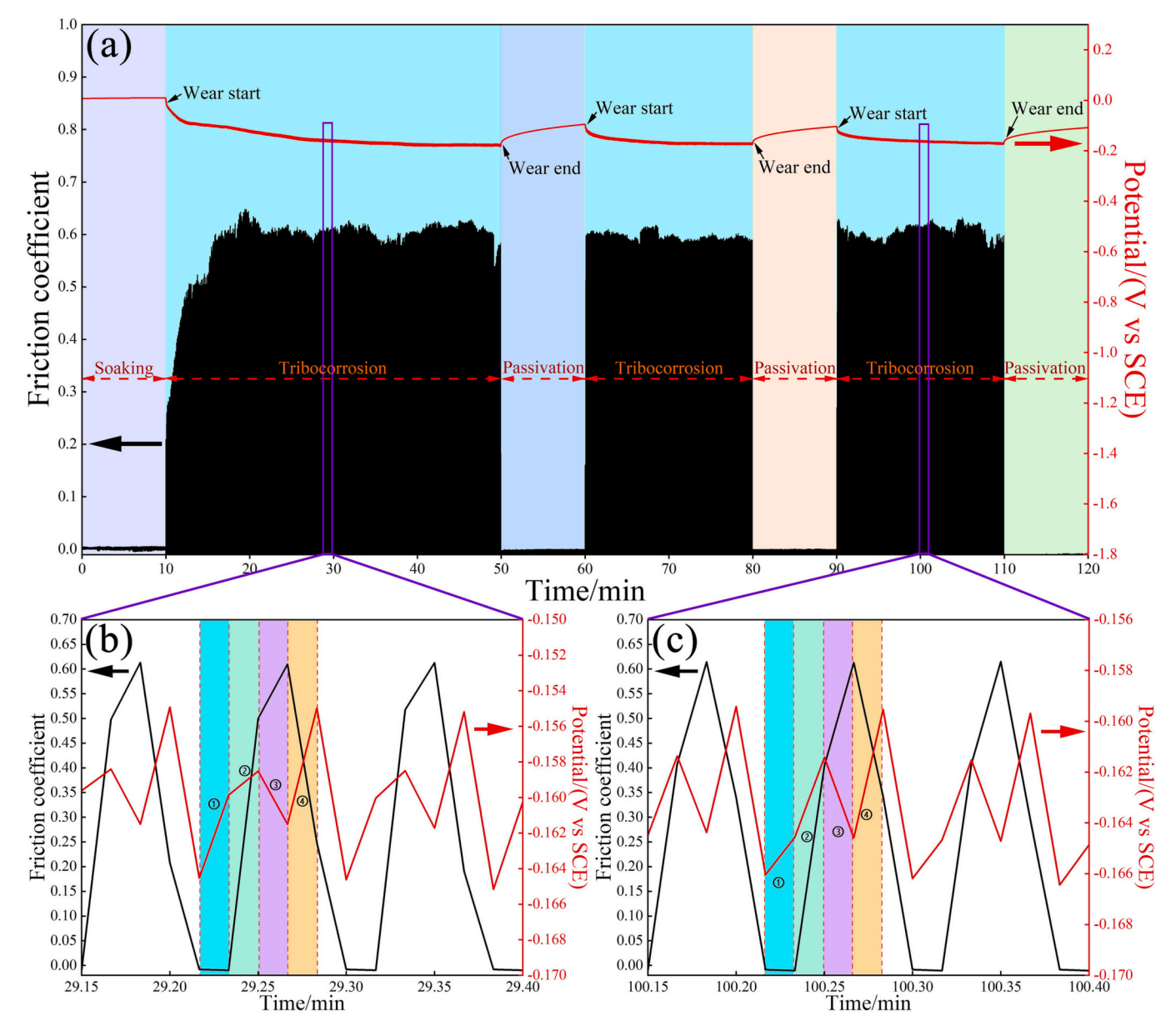


Fig. 9. (a) Tribocorrosion curves and the corresponding OCP of $(Mo_{0.8}Cr_{0.2})_5Si_3$ alloy with a vibration frequency of 0.2 Hz in 3.5 wt% NaCl solution; (b and c) Partial magnification of the tribocorrosion curves and OCP for different cycle tests.

3.3. Tribocorrosion behaviors of $(Mo_{1-x}Cr_x)_5Si_3$ alloys

To ensure surface electrochemical stability, the alloys were soaked in NaCl solution for 10 h prior to the electrochemical corrosion and tribocorrosion test. Three specimens (10 mm \times 10 mm \times 5 mm) of each alloy were prepared to ensure the accuracy of the test results. Fig. 7 shows the open circuit potential and potentiodynamic polarization curves of (Mo_{1-x}Cr_x)₅Si₃ alloys in 3.5 wt% NaCl solution. Compared with the Mo_5Si_3 alloy, the OCP values of the $(Mo_{0.8}Cr_{0.2})_5Si_3$ and (Mo_{0.6}Cr_{0.4})₅Si₃ alloys are more positive and stable over time as shown in Fig. 7 (a). From Fig. 7 (b), the obvious passivation regions are observed in the anodic polarization of the $(Mo_{1-x}Cr_x)_5Si_3$ (x = 0, 0.2, 0.4) alloys. However, the Cr-alloyed (Mo_{1-x}Cr_x)₅Si₃ alloys have a wider passivation range and a lower passivation current density than the Mo₅Si₃ sample. Table 2 shows the values of major electrochemical parameters obtained from the polarization curves. Actually, the corrosion potential E_{corr} predicts the possibility of alloy corrosion to some extent, and the corrosion current density i_{corr} can directly indicate the corrosion rate of the material during the electrochemical corrosion. From Table 2,

with increasing the Cr content, $(Mo_{1-x}Cr_x)_5Si_3$ alloys have a much more positive corrosion potential (E_{corr}) and breakdown potential (E_b) , and a relatively stable corrosion current (i_{corr}) . Therefore, the electrochemical corrosion resistance of $(Mo_{1-x}Cr_x)_5Si_3$ alloy can be significantly improved by Cr alloying.

Fig. 8 shows the variation of friction coefficients and open circuit potential (OCP, vs SCE) values of $(Mo_{1-x}Cr_x)_5Si_3$ alloys sliding against Al_2O_3 balls in 3.5 wt% NaCl solution before, during and after the tribocorrosion test. It is obvious that the variation of OCP values for the $(Mo_{1-x}Cr_x)_5Si_3$ alloys is ignored during immersion. This indicates that a stable electrochemical state was obtained on the surface of the alloys. Moreover, the OCP values of the alloys increase with increasing Cr content, indicating that the Cr alloying improves the corrosion resistance of the Mo_5Si_3 alloy. In contrast, the OCP value of OCr18Ni9 is higher, indicating better electrochemical stability in a static corrosion environment than the $(Mo_{1-x}Cr_x)_5Si_3$ alloys. However, once the sliding starts, the OCP value of OCr18Ni9 drops dramatically to a more negative value than that of the $(Mo_{1-x}Cr_x)_5Si_3$ alloys. This suggests that the stable passivation film on the surface was destroyed by mechanical friction.

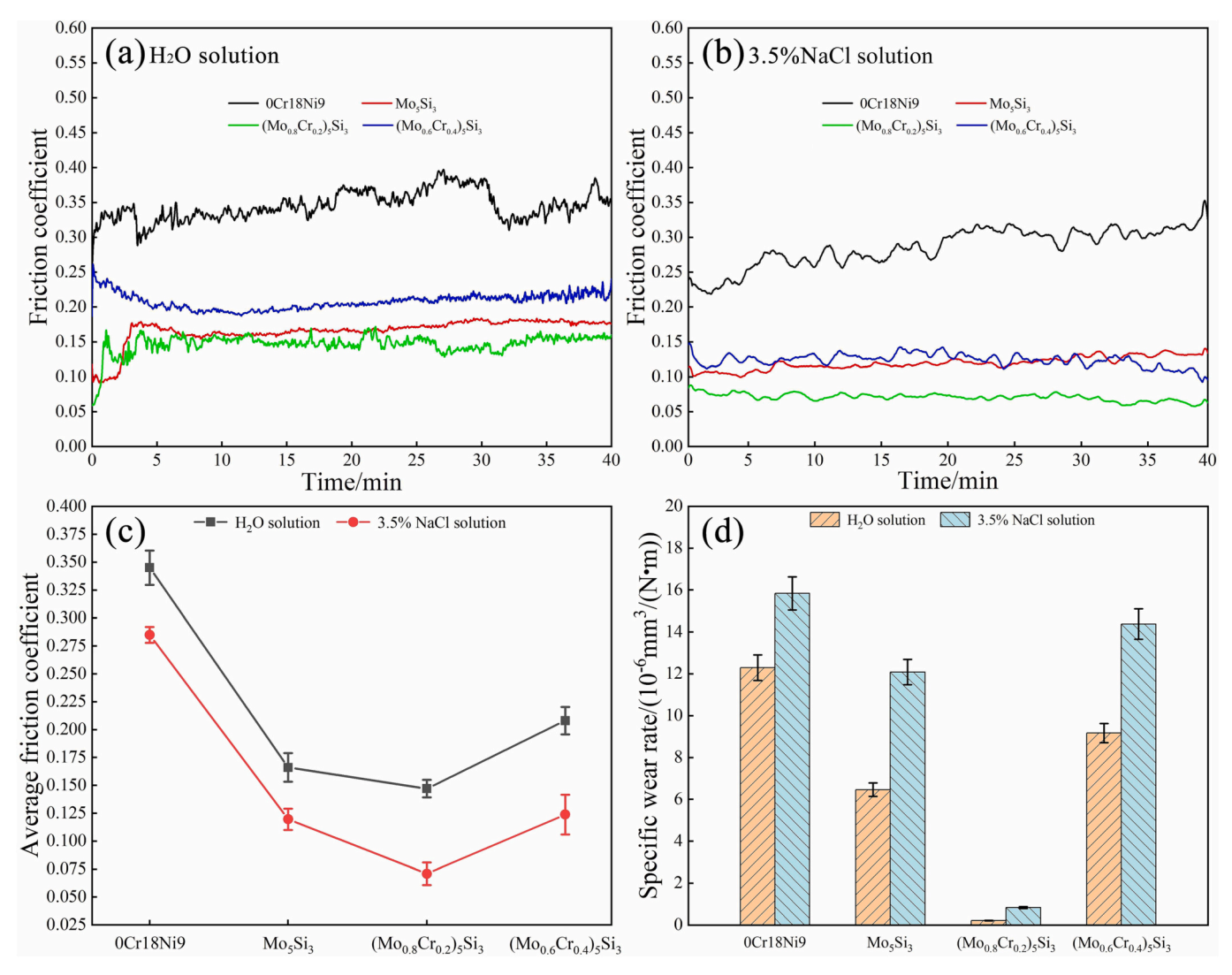


Fig. 10. Average friction coefficients and wear rates of OCr08Ni9 and (Mo_{1.x}Cr_x)₅Si₃ (x = 0,0.2,0.4) alloys in deionized water and 3.5 wt% NaCl solution.

The electrochemical activity of the fresh wear track (as an anode) of 0Cr18Ni9 was higher than that of the unworn passivated surface (as a cathode), which easily leads to galvanic corrosion due to the potential difference of the material surface. Therefore, the average OCP value of 0Cr18Ni9 drops dramatically from 0.5~V to -0.21~V. In comparison, the OCP values of (Mo_{1-x}Cr_x)₅Si₃ alloys decreased slightly and remained more stable than OCr18Ni9 stainless steel. The OCP values of Mo₅Si₃, $(Mo_{0.8}Cr_{0.2})_5Si_3$ and $(Mo_{0.6}Cr_{0.4})_5Si_3$ alloys during the tribocorrosion were -0.16 V, -0.18 V and -0.19 V, respectively. Apparently, the OCP values of the (Mo_{1-x}Cr_x)₅Si₃ alloys were more positive than those of the OCr18Ni9 material. Moreover, unlike static corrosion, the OCP values of the (Mo_{1-x}Cr_x)₅Si₃ alloys decreased with increasing Cr content during tribocorrosion. Under static corrosion conditions, the introduction of Cr elements easily leads to the formation of a stable Cr₂O₃ passivation film on the surface of the alloys, which improves the corrosion resistance. However, during the tribocorrosion process, it was difficult to establish a stable passivation state on the surface. Tribocorrosion resistance of the material mainly depends on (1) the balance between the removal rate of the passivation film and the re-passivation ability, and (2) the inherent mechanical and chemical properties of the surface. Therefore, (Mo1. _xCr_x)₅Si₃ alloys exhibited a better tribocorrosion resistance than 0Cr18Ni9 material due to their uniform composition, high hardness, strong covalent bonding characteristics and good chemical stability. Once the sliding stopped, the OCP values of all samples increased to higher values, indicating that a new passivation film was formed on the surface of the samples. As shown in Fig. 8, the average friction coefficients of Mo $_5$ Si $_3$ /Al $_2$ O $_3$, (Mo $_0.8$ Cr $_0.2$) $_5$ Si $_3$ /Al $_2$ O $_3$, (Mo $_0.6$ Cr $_0.4$) $_5$ Si $_3$ /Al $_2$ O $_3$ and 0Cr18Ni9/Al $_2$ O $_3$ tribopairs were 0.119, 0.071, 0.124 and 0.285, respectively. It was evident that all the average friction coefficients of the (Mo $_{1-x}$ Cr $_x$) $_5$ Si $_3$ /Al $_2$ O $_3$ tribopairs were lower and more stable than those of the 0Cr18Ni9/Al $_2$ O $_3$ tribopairs, indicating excellent tribological properties of the (Mo $_{1-x}$ Cr $_x$) $_5$ Si $_3$ alloys in the 3.5 wt% NaCl solutions.

To further elucidate the tribocorrosion characteristics and wear-corrosion combined effects of the samples during the reciprocating sliding, Fig. 9 (a) shows the tribocorrosion curves and the corresponding OCP for the $(Mo_{0.8}Cr_{0.2})_5Si_3$ alloy at a low vibration frequency of 0.2 Hz in 3.5 wt% NaCl solution. The tribocorrosion curves and OCP exhibit almost similar features in all cycle tests. This suggests that the tribocorrosion characteristics of the $(Mo_{0.8}Cr_{0.2})_5Si_3$ alloy are stable in 3.5 wt% NaCl solution. In Fig. 9 (a), the OCP value of the $(Mo_{0.8}Cr_{0.2})_5Si_3$ alloy remains relatively stable with time, which is consistent with the trend of the OCP of the alloy under static corrosion conditions in Fig. 7 (a). It is worth noting that a good correlation between the friction coefficient and the OCP at different stages of one sliding amplitude cycle of the $(Mo_{0.8}Cr_{0.2})_5Si_3$ alloy was observed in Fig. 9 (b and c) for stages 1-4. The OCP value increases when sliding stops (stage 1 and 2) due to the re-passivation of the worn surface. Then the OCP value drops

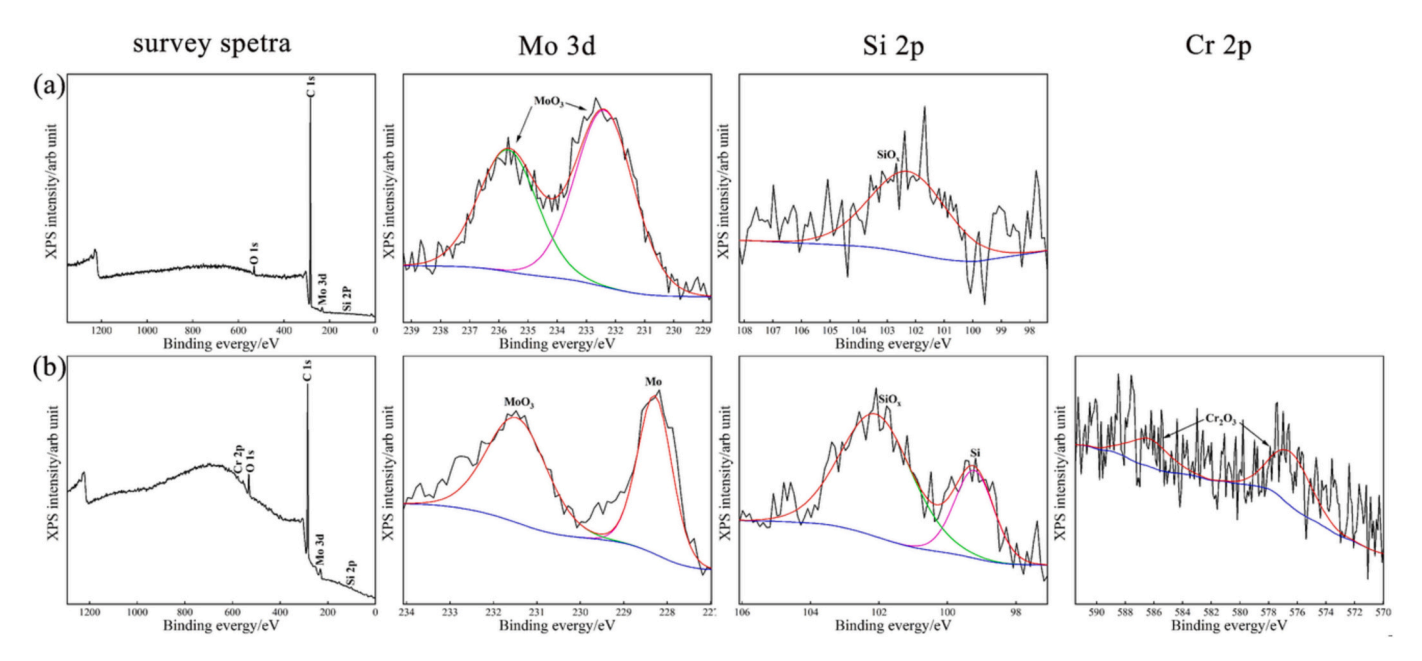


Fig. 11. XPS survey spectra and high-resolution XPS spectra of Mo_5Si_3 (a) and $(Mo_{0.8}Cr_{0.2})_5Si_3$ (b) alloys surface after tribocorrosion testing in 3.5 wt% NaCl solution.

dramatically (stage 3) due to the damage of the surface passivation film caused by the sliding. Subsequently, in stage 4, the OCP value increases again with the friction coefficient gradually reducing to zero. This phenomenon can be attributed to the interaction of wear and corrosion of the alloy during the tribocorrosion process [8,35].

Fig. 10 (a and b) shows the friction coefficients of OCr08Ni9 and (Mo_{1-x}Cr_x)₅Si₃ alloys sliding against Al₂O₃ balls in deionized H₂O solution and 3.5 wt% NaCl solution. Average friction coefficients of (Mo₁. $_{x}Cr_{x})_{5}Si_{3}$ (x = 0, 0.2, 0.4)/Al₂O₃ tribopairs in deionized water and 3.5 wt % NaCl solutions were (0.166, 0.147, 0.208) and (0.119, 0.071, 0.124), respectively. While the average friction coefficients of OCr08Ni9/Al₂O₃ tribopairs were 0.345 and 0.285 in both solutions, which were significantly higher than those of (Mo_{1-x}Cr_x)₅Si₃ alloys. Ma et al. [36] pointed out that the friction coefficient was mainly affected by the surface roughness and surface lubrication, assuming all other test conditions were identical. OCr08Ni9 is a passive material. It is insensitive to corrosion due to the presence of a dense passive film on the surface. However, the surface corrosion and wear of 0Cr08Ni9 became more severe during the tribocorrosion test due to the breakdown of the passivation film. The high hardness of the wear debris on the wear track further accelerates the abrasive wear and corrosion (in Fig. 10 (a2)), which increases the roughness of the OCr08Ni9 surface. Therefore, the friction coefficient of 0Cr08Ni9 is higher and gradually increases with sliding time. In contrast, the (Mo_{1-x}Cr_x)₅Si₃ alloys have excellent chemical stability and high hardness, and their surface roughness changes are relatively mild. The COF of (Mo_{1-x}Cr_x)₅Si₃ alloys is mainly affected by surface lubrication. According to the XPS results of the tribocorrosion surface of the Mo_5Si_3 and $(Mo_{0.8}Cr_{0.2})_5Si_3$ alloy in Fig. 11, the surfaces of the alloys were mainly composed of Mo, Si, Cr and O elements, and an oxide film (MoO_3 , Cr_2O_3 and SiO_x) was formed on the surface of the (Mo_{1-x}Cr_x)₅Si₃ alloys during the tribocorrosion test and provides a good lubricating effect, which was consistent with the results of Xu and Fu [12,37].

$$(Mo_{1-x}Cr_x)_5Si_3 + H_2O \rightarrow MoO_3 + Cr_2O_3 + SiO_2$$
 (3)

As a result, the $(Mo_{1-x}Cr_x)_5Si_3$ alloys exhibited a low friction coefficient compared to OCrO8Ni9. In Fig. 10 (c), the average friction coefficients of all samples in NaCl solution are lower than that in deionized water. This is mainly attributed to the fact that surface transfer films with good lubricity are more easily formed in NaCl solution under the

combined effect of wear and corrosion during the tribocorrosion process. However, the combined effect of wear and corrosion (wear accelerates corrosion, corrosion promotes wear) also led to the high wear rate of the materials in NaCl solution, as shown in Fig. 10 (d). It can be seen that the wear rate and friction coefficient of the samples show a consistent tendency to change. The wear rates of the (Mo_{1-x}Cr_x)₅Si₃ alloys are lower than those of the 0Cr08Ni9 stainless steel. It has been reported that MoO₃ acts as a lubricant to reduce the friction coefficient and wear rate, while MoO₃ and Cr₂O₃ act as a corrosion barrier to reduce the corrosion rate [38,39], which contributes to improving the tribocorrosion resistance of (Mo_{1-x}Cr_x)₅Si₃ alloys. In addition, the high hardness, strong covalent bonding and good chemical stability of (Mo₁, _xCr_x)₅Si₃ alloys also make them present better tribocorrosion characteristics compared to 0Cr08Ni9 material. Among all alloys, the (Mo_{0.8}Cr_{0.2})₅Si₃ alloy exhibits the best tribocorrosion performance with a low COF and wear rate. The wear rates of the (Mo_{0.8}Cr_{0.2})₅Si₃ alloy were 0.21×10^{-6} mm³/N·m and 0.83×10^{-6} mm³/N·m in deionized water and 3.5 wt% NaCl solution, respectively, which were almost two orders of magnitude lower than those of the other alloys. This may be related to the high H/E ratio, low thermal expansion anisotropy (CTE (c)/CTE(a)) and consistent microstructure of the (Mo_{0.8}Cr_{0.2})₅Si₃ alloy.

Fig. 12 shows the SEM images and worn section profiles of wear tracks on 0Cr08Ni9 and (Mo_{1-x}Cr_x)₅Si₃ alloys after the tribocorrosion test. The wear track width and cross-sectional area of all samples are significantly larger after tribocorrosion in 3.5 wt% NaCl solution than those in deionized water, indicating a strong corrosion-accelerated wear effect. In Fig. 12 (a1-a2), the OCrO8Ni9 stainless steel is subjected to severe corrosion and wear on its surface, and some corrosion and wear products adhere to the wear surface, making the wear tracks more visible. In contrast, the alloy is a brittle material with excellent corrosion and wear resistance, which is prone to brittle spalling during the tribocorrosion process, and the products are not easily adhered to the surface, making the wear tracks less visible. In Fig. 12 (b1-b2), severe spalling and cracking of the Mo₅Si₃ alloy during tribocorrosion can be mainly attributed to high residual thermal stress (high thermal expansion anisotropy) and fatigue fracture induced by reciprocating sliding. Compared to the Mo₅Si₃ alloy, the wear tracks of the (Mo_{0.8}Cr_{0.2})₅Si₃ alloy were relatively smooth without significant peeling off, and only slight corrosion and cracks were present at the phase interface as shown in Fig. 12 (c1-c2). The EDS analyses were performed at point A and point

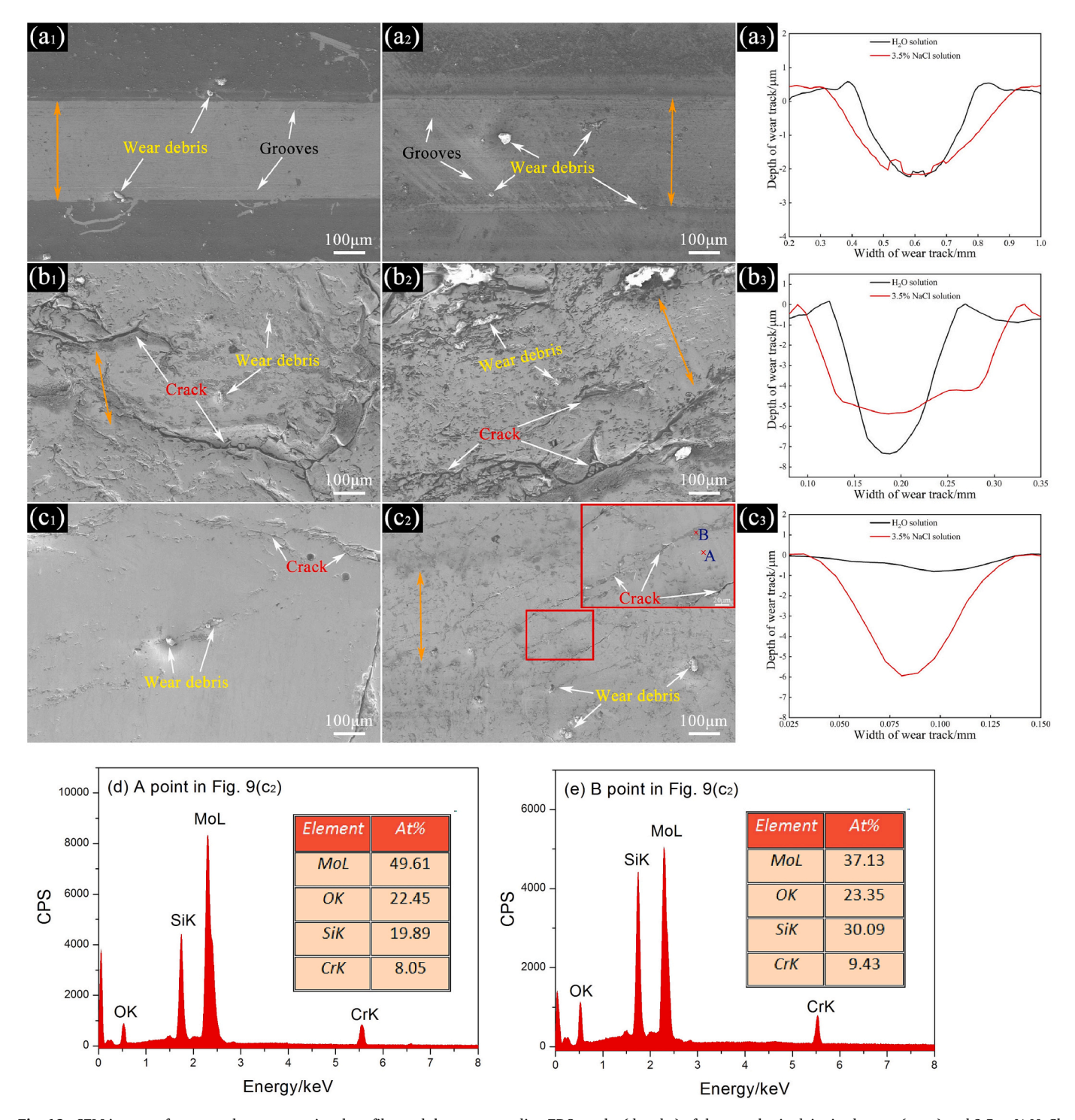


Fig. 12. SEM images of wear tracks, cross-sectional profiles and the corresponding EDS results (d and e) of the samples in deionized water (a_1-c_1) and 3.5 wt% NaCl solution (a_2-c_2) . (a_1-a_3) 0Cr08Ni9, (b_1-b_3) Mo₅Si₃, (c_1-c_3) (Mo_{0.8}Cr_{0.2})₅Si₃.

B, located on the smooth surface and tribocorrosion products, respectively (Fig. 12 (d and e)). The elements Mo, Si, Cr and O were detected at both points, but the content of O and Si elements at point B was higher than that at point A. This indicates that selective tribocorrosion of the intergranular phase (MoSi₂) occurred on the surface of the (Mo_{0.8}Cr_{0.2}) $_5$ Si₃ alloy during the tribocorrosion test in NaCl solution.

Fig. 13 shows the typical TEM, HRTEM images, and SAED pattern of wear debris from $(Mo_{0.8}Cr_{0.2})_5Si_3$ alloy after the tribocorrosion test in 3.5 wt% NaCl solution. The wear debris exhibited a nanocrystalline structure and composed of Mo_5Si_3 and $MoSi_2$ dual phases, which was

confirmed by its corresponding SAED pattern in Fig. 13 (b). In Fig. 13 (c), the lattice spacings of the wear debris were 0.2326 nm, 0.2318 nm and 0.1999 nm, which were consistent with the (321) and (112) planes of Mo_5Si_3 (PDF No. 65–2783) and the (200) plane of $MoSi_2$ (PDF No. 17–0917), respectively.

3.4. Material loss and tribocorrosion mechanisms of $(Mo_xCr_{1-x})_5Si_3$ alloys

In the tribocorrosion process, the material loss due to the combined

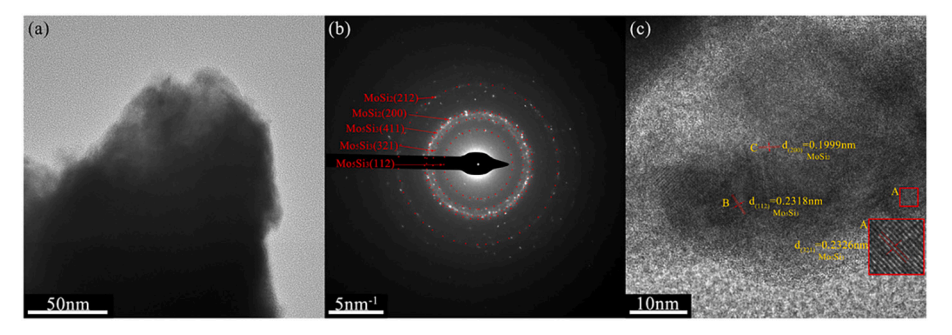


Fig. 13. TEM (a), corresponding SAED pattern (b) and HRTEM images (c) of wear debris for (Mo_{0.8}Cr_{0.2})₅Si₃ alloy in 3.5 wt% NaCl solution.

Table 3 Loss volumes of total tribocorrosion (V_t) , pure wear (V_w) , corrosion-induced wear (V_{cm}) , pure corrosion and wear-induced corrosion $(V_c + V_{mc})$ of the samples after tribocorrosion tests.

Samples	$V_t (\mathrm{mm}^3)$	$V_w (\text{mm}^3)$	$V_c + V_{mc} (\mathrm{mm}^3)$	$V_{cm} (\mathrm{mm}^3)$
0Cr18Ni9	3.8 E - 3	2.95 E - 3	8.07 E - 5	7.69 E – 4
Mo_5Si_3	2.9 E - 3	1.55 E - 3	3.27 E - 5	1.32 E - 3
$(Mo_{0.8}Cr_{0.2})_5Si_3$	0.2 E - 3	5.06 E - 5	0.89 E - 5	1.41 E - 4

effect of wear and corrosion could be calculated using the formula (4) proposed by Watson et al. [40]:

$$V_t = V_w + V_c + V_{wc} + V_{cw} (4)$$

Here, V_t is the total material loss from tribocorrosion, V_w is pure mechanical wear (sliding in deionized water), V_c is corrosion-only without wear, V_{wc} is wear-induced corrosion, and V_{cw} is corrosion-induced wear. The V_t and V_w were determined using a surface profilometer to examine the wear scar cross-sectional area (obtained from Fig. 12 (a3, b3 and c3), V = LS, L is the sliding amplitude (5 mm), S is the cross-section area of the wear scars). The results of the calculations are presented in Table 3. The high-resolution inductively coupled plasma optical emission spectrometer (ICP-OES) technique is widely used in the corrosion and chemical industries due to its high detection accuracy. M. T. Mathew et al. [41] comparisons of the tribocorrosion loss of CoCrMo alloy after the tribocorrosion test in NaCl solution was carried out using the wear scar profile method and the total metal content method (ICP-MS), respectively. The results showed good consistency between the two

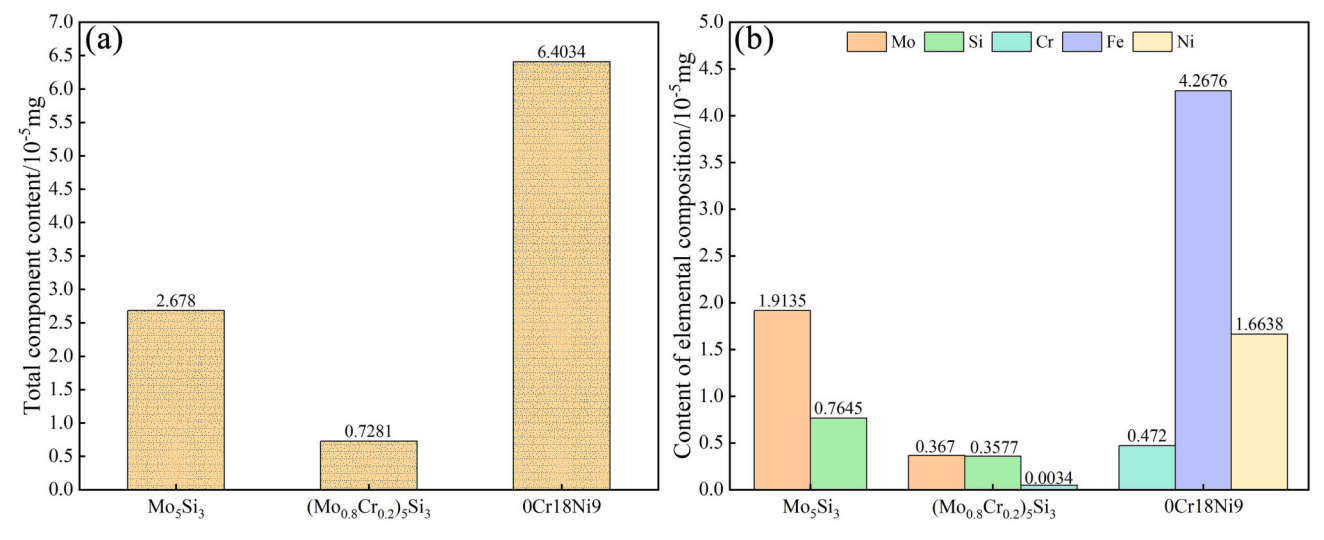


Fig. 14. ICP-OES elemental component analysis of the samples solution after tribocorrosion test. (a) Total component content, (b) Content of elemental components.

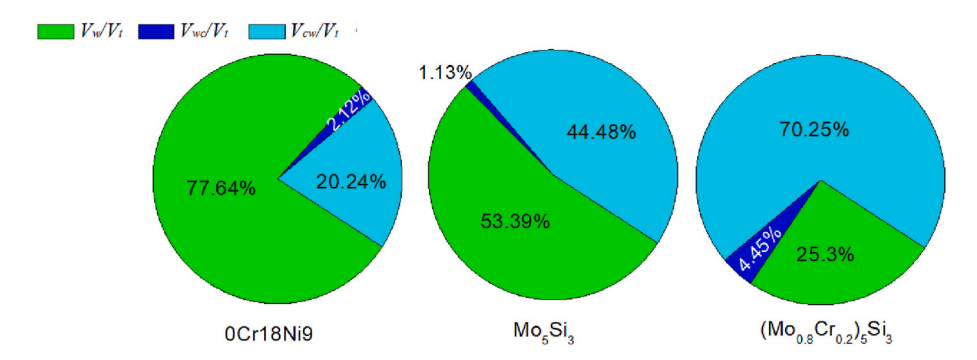


Fig. 15. Contributions of tribocorrosion components for 0Cr18Ni9, Mo_5Si_3 and $(Mo_{0.8}Cr_{0.2})_5Si_3$ alloys sliding against Al_2O_3 balls under OCP conditions in 3.5 wt% NaCl solution.

techniques. However, a small proportion of metal ions may precipitate during the tribocorrosion process that cannot be detected by ICP-MS technology, resulting in slightly lower measured values for tribocorrosion loss. To promote the dissolution of metal ions, the samples and solutions after the tribocorrosion test were subjected to ultrasonic vibration and cleaning, but this may still not be sufficient. Then, some solutions (about 1/10th of the total) were extracted and analyzed the component content by the ICP-OES method, and the results are shown in Fig. 14. In Fig. 14 (a), it can be observed that the (Mo_{0.8}Cr_{0.2})₅Si₃ alloy had the lowest component content in the tribocorrosion solutions, which was almost an order of magnitude lower than that of the Mo₅Si₃ and OCr18Ni9 stainless steel. This indicated that (Mo_{0.8}Cr_{0.2})₅Si₃ alloy has better corrosion and tribocorrosion resistance than that of 0Cr18Ni9. According to Fig. 14 (a), V_c and V_{wc} were calculated (V = m/ ρ , where m is the metal content in the solution, and ρ is the material density) and the results are presented in Table 3. Fig. 14 (b) shows the content of each element in the sample solution after the tribocorrosion test. It was worth noting that the contents of Mo and Si elements in the tribocorrosion solution of the $(Mo_{0.8}Cr_{0.2})_5Si_3$ alloy were $0.367 \diamondsuit 10^{-5}$ mg and $0.358 \triangle 10^{-5}$ mg, respectively. The high Si content was attributed to the fact that the Cr alloying promoted the formation of the MoSi₂ phase with high Si content at the grain boundaries, which facilitated the formation of primary cells and accelerated the corrosion and tribocorrosion of the MoSi₂ intergranular phase. V_{cw} cannot be directly detected, but it can be obtained using the formula (5), the results are presented in Table 3.

$$V_{cw} = V_t - V_w - V_c - V_{wc} (5)$$

As shown in Fig. 15, the 0Cr18Ni9 and Mo₅Si₃ alloys have a high percentage of pure wear material loss, and their percentage of V_w is 77.64% and 53.39%, respectively. This indicates that the pure wear (V_w) was the main factor of material loss for 0Cr18Ni9 and Mo₅Si₃ alloy. For all samples, the amount of material volume loss caused by pure corrosion (V_c) and wear-induced corrosion (V_{wc}) was very small. Moreover, as a passivated material, the outer part of the wear track was protected by the passive layer, and the material loss caused by pure corrosion (V_c) was neglected [40]. Thus, the material loss (V_{wc}) percentages of 0Cr18Ni9, Mo_5Si_3 and $(Mo_{0.8}Cr_{0.2})_5Si_3$ alloy were 2.12%, 1.13% and 4.45%, respectively. For the (Mo_{0.8}Cr_{0.2})₅Si₃ alloy, the percentage of wear-corrosion combined (V_{cw} and V_{wc}) was 74.7%, indicating that the wear-corrosion combined effect was the main contributor to material loss. Furthermore, among the wear-corrosion combined (V_{cw} and V_{wc}), the corrosion-induced wear (V_{cw}) was much larger than wear-induced corrosion (Vwc) for all three materials, suggesting that corrosioninduced wear was the main tribocorrosion mechanism.

4. Conclusions

The microstructure and tribocorrosion behaviors of 0Cr18Ni9 stainless steel and $(Mo_{1-x}Cr_x)_5Si_3$ alloys were investigated in 3.5 wt% NaCl solution, and the following conclusions were drawn:

- (1) The microstructure characteristics and mechanical properties of Mo₅Si₃ alloy were enhanced by Cr alloying. With the increase of Cr content, the lattice thermal expansion anisotropy (CTE (c)/CTE (a)) of (Mo_{1-x}Cr_x)₅Si₃ alloys decreased from 2.21 to 1.45. The (Mo_{1-x}Cr_x)₅Si₃ alloys exhibited a uniform and refined structure, low internal stresses, high fracture toughness and H/E values.
- (2) During the tribocorrosion tests, a continuous inverse relationship between friction coefficient and OCP values was observed for $(Mo_{1-x}Cr_x)_5Si_3$ alloys, showing a strong wear-corrosion combined effect. Due to the formation of the Cr_2O_3 - MoO_3 - SiO_x multiphase protective film, the corrosion and tribocorrosion resistance of $(Mo_{1-x}Cr_x)_5Si_3$ alloys was better than that of OCr18Ni9 stainless steel in 3.5 wt% NaCl solution. $(Mo_{0.8}Cr_{0.2})_5Si_3$ alloy has the best tribocorrosion characteristics with a low friction coefficient and wear rate.

(3) For the 0Cr18Ni9 and Mo_5Si_3 alloy, pure wear (V_w) was a dominant position in material loss. However, the wear loss of $(Mo_{0.8}Cr_{0.2})_5Si_3$ alloy was mainly attributed to the combined effect of wear and corrosion $(V_{cw}$ and $V_{wc})$, and corrosion-induced wear (V_{cw}) was the main tribocorrosion mechanism.

CRediT authorship contribution statement

R.P. Li: Formal analysis, Investigation, Writing - original draft, Writing - review & editing. **H. Chen:** Formal analysis, Investigation, Funding acquisition, Writing - review & editing. **X.H. Hao:** Investigation, Writing - original draft. **B.X. Huang:** Investigation.

Declaration of Competing Interest

The authors declare that they have no known competing financial interests or personal relationships that could have appeared to influence the work reported in this paper.

Data availability

The raw/processed data required to reproduce these findings cannot be shared at this time as the data also forms part of an ongoing study.

Acknowledgments

This research was supported by the Natural Science Foundation of Shandong Province of China (Grant Nos. ZR2021ME204 and ZR2020QE004). The authors acknowledge Mr. Deshun Liu for their assistance in the experiments of the nanoindentation test.

References

- [1] N. Hou, N. Ding, S. Qu, W.M. Guo, L. Liu, N. Xu, L.N. Tian, H.X. Xu, X.F. Chen, F. Zaïri, C.-M. Lawrence Wu, Failure modes, mechanisms and causes of shafts in mechanical equipment, Eng. Fail. Anal. 136 (2022), 106216.
- [2] M.A. Hoque, C.W. Yao, M. Khanal, I. Lian, Tribocorrosion behavior of micro/ nanoscale surface coatings, Sensors 22 (2022) 9974.
- [3] M. Salasi, G.B. Stachowiak, G.W. Stachowiak, New experimental rig to investigate abrasive-corrosive characteristics of metals in aqueous media, Tribol. Lett. 40 (2010) 71–84.
- [4] S. Cao, S. Mischler, Modeling tribocorrosion of passive metals a review, Curr. Opin. Solid State Mater. Sci. 22 (2018) 127–141.
- [5] Z.Y. Li, H.Y. Yu, D.B. Sun, The tribocorrosion mechanism of aluminum alloy 7075-T6 in the deep ocean, Corros. Sci. 183 (2021), 109306.
- [6] H. Chen, Z. Zhang, X.H. Hao, B.X. Huang, X.C. Zhao, C.C. Hu, Microstructure and tribocorrosion properties of NiTi/AlNi₂Ti ternary intermetallic alloy, Vacuum 184 (2021), 109928.
- [7] L.X. Dong, H.M. Wang, Microstructure and corrosion properties of laser-melted deposited Ti₂Ni₃Si/NiTi intermetallic alloy, J. Alloys Compd. 465 (2008) 83–89.
- [8] Q. Chen, Y.Z. Gao, Z.W. Xie, T. Chen, Y.Y. Wan, H. Wang, X. Gao, Y. Chen, Y. W. Zhou, Y.Y. Guo, Tribocorrosion behaviors of CrN coating in 3.5 wt% NaCl solution, Thin Solid Films 622 (2017) 41–47.
- [9] L. Ceschini, C. Chiavari, E. Lanzoni, C. Martini, Low-temperature carburized AISI 316L austenitic stainless steel: wear and corrosion behaviour, Mater. Des. 38 (2012) 154–160.
- [10] T. Zhao, S. Zhang, Z.Y. Wang, C.H. Zhang, D.X. Zhang, N.W. Wang, C.L. Wu, Cavitation erosion/corrosion synergy and wear behaviors of nickel-based alloy coatings on 304 stainless steel prepared by cold metal transfer, Wear 510-511 (2022), 204510.
- [11] A.H. Kasama, A.J. Mourisco, C.S. Kiminami, W.J. Botta, F.C. Bolfarini, Microstructure and wear resistance of spray formed high chromium white cast iron, Mater. Sci. Eng. A 375–377 (2004) 589–594.
- [12] J. Xu, C.H. Zhou, S.Y. Jiang, Investigation on corrosion behavior of sputter-deposited nanocrystalline (Mo_xCr_{1-x})₅Si₃ films by double cathode glow plasma, Intermetallics 18 (2010) 1669–1675.
- [13] T.M. Yue, H. Zhang, Microstructure and wear resistance of compositionally graded Ti-Si laser-clad coatings, Mater. Res. Innov. 19 (2015) 9–13.
- [14] G. Duan, H.M. Wang, High-temperature wear resistance of a laser-clad γ/Cr₃Si metal silicide composite coating, Scr. Mater. 46 (2002) 107–111.
- [15] M.Y. Niu, X.H. Zhang, J.J. Chen, X.Y. Yang, Friction and wear properties of Ni₃Si alloy under different vacuum conditions, Vacuum 161 (2019) 443–449.
 [16] H. Matsunoshita, Y. Sasai, K. Fujiwara, K. Kishida, H. Inui, Plastic deformation of
- [16] H. Matsunoshita, Y. Sasai, K. Fujiwara, K. Kishida, H. Inui, Plastic deformation of directionally solidified ingots of binary and some ternary MoSi₂/Mo₅Si₃ eutectic composites, Sci. Technol. Adv. Mater. 17 (2016) 517–529.

- [17] O. Kazemi, G. Hasemann, M. Krüger, T. Halle, Microstructure evolution and sequence of phase transition reactions through the solidification of Mo-Si-B alloy; a phase-field study, Comput. Mater. Sci. 193 (2021), 110422.
- [18] Y. Pan, P. Wang, C.M. Zhang, Structure, mechanical, electronic and thermodynamic properties of Mo₅Si₃ from first-principles calculations, Ceram. Int. 44 (2018) 12357–12362.
- [19] E. Ström, S. Eriksson, H. Rundlöf, J. Zhang, Effect of site occupation on thermal and mechanical properties of ternary alloyed Mo₅Si₃, Acta Mater. 53 (2005) 357–365.
- [20] W.J. Choi, S.Y. Lee, C.W. Park, J.H. Park, J.M. Byun, Y.D. Kim, Effect of titanium addition on mechanical properties of Mo-Si-B alloys, Int. J. Refract. Met. H 80 (2019) 238–242.
- [21] C. Zenk, J.S.K.L. Gibson, V. Maier-Kiener, S. Neumeier, M. Goken, S. Korte-Kerzel, Low temperature deformation of MoSi₂ and the effect of Ta, Nb and Al as alloying elements, Acta Mater. 181 (2019) 385–398.
- [22] T. Yang, X.P. Guo, Effects of Nb content on the mechanical alloying behavior and sintered microstructure of Mo-Nb-Si-B alloys, Metals 9 (2019) 653.
- [23] M.A. Azim, H.J. Christ, B. Gorr, T. Kowald, O. Lenchuk, K. Albe, M. Heilmaier, Effect of Ti addition on the thermal expansion anisotropy of Mo₅Si₃, Acta Mater. 132 (2017) 25–34.
- [24] E. Ström, J. Zhang, S. Eriksson, C.H. Li, D. Feng, The influence of alloying elements on phase constitution and microstructure of Mo₃M₂Si₃(M=Cr, Ti, Nb, Ni, or Co), Mat. Sci. Eng. A 329-331 (2002) 289–294.
- [25] C.B. Tang, F.R. Wen, H.X. Chen, J.J. Liu, G.Y. Tao, X.J. Xu, J.Q. Xue, Corrosion characteristics of Fe₃Si intermetallic coatings prepared by molten salt infiltration in sulfuric acid solution, J. Alloys Compd. 778 (2019) 972–981.
- [26] Y.G. Wang, J.L. Liu, Corrosion of barium aluminosilicates by water-vapor: an investigation from first principles, Corros. Sci. 51 (2009) 2126–2129.
- [27] H. Chen, Q. Ma, X. Shao, J. Ma, B.X. Huang, Corrosion and microstructure of the metal silicide (Mo_{1-x}Nb_x)₅Si₃, Corros. Sci. 70 (2013) 152–160.
- [28] J. Xu, Z.Y. Li, P. Munroe, Z.H. Xie, Role of Cr additions in enhancing wear and oxidation resistance of (Mo_{1-x}Cr_x)Si₂ nanocrystalline films, Ceram. Int. 40 (2014) 15859–15874.
- [29] J. Xu, L.L. Liu, Z.Y. Li, P. Munroe, Z.H. Xie, Effect of Al addition upon mechanical robustness and corrosion resistance of Mo₅Si₃/ MoSi₂ gradient nanocomposite coatings, Surf. Coat. Technol. 223 (2013) 115–125.

- [30] J.L. Chai, Y.B. Zhu, T.L. Shen, Y.W. Liu, L.J. Niu, S.F. Li, P. Jin, M.H. Cui, Z. G. Wang, Assessing fracture toughness in sintered Al₂O₃-ZrO₂(3Y)-SiC ceramic composites through indentation technique, Ceram. Int. 46 (2020) 27143–27149.
- [31] W.C. Oliver, G.M. Pharr, An improved technique for determining hardness and elastic-modulus using load and displacement sensing indentation experiments, J. Mater. Res. 7 (1992) 1564–1583.
- [32] C.L. Fu, J.H. Schneibel, Reducing the thermal expansion anisotropy in Mo₅Si₃ by Nb and V additions: theory and experiment, Acta Mater. 51 (2003) 5083–5092.
- [33] J. Xu, J.D. Wu, D.H. Lai, Z.H. Xie, P. Munroe, Investigation on the effect of alloying elements on mechanical properties of MoSi₂ by first principle calculation, Mater. Sci. Technol. 28 (2012) 1337–1344.
- [34] M.D. Zhang, F. Zhou, Q.Z. Wang, Y.Q. Fu, Z.F. Zhou, Tribocorrosion characteristics of CrMoSiCN/Ag coatings on Ti6Al4V alloys in seawater, Ceram. Int. 47 (2021) 31780–31797.
- [35] Z.W. Xie, T. Chen, Q. Chen, Q. Yang, S. Tan, Y.J. Wang, Y.M. Luo, Z.Z. Luo, M. Q. Hua, Tribocorrosion behaviors of AlN/MoS₂-phenolic resin duplex coatings on nitrogen implanted magnesium alloys, Surf. Coat. Technol. 266 (2015) 64–69.
- [36] F.L. Ma, J.L. Li, Z.X. Zeng, Y.M. Gao, Structural, mechanical and tribocorrosion behaviour in artificial seawater of CrN/AlN nano-multilayer coatings on F690 steel substrates, Appl. Surf. Sci. 428 (2018) 404–414.
- [37] Y.Q. Fu, F. Zhou, Q.Z. Wang, M.D. Zhang, Z.F. Zhou, Electrochemical and tribocorrosion performances of CrMoSiCN coating on Ti-6Al-4V titanium alloy in artificial seawater, Corros. Sci. 165 (2020), 108385.
- [38] M.D. Zhang, F. Zhou, Q.Z. Wang, Y.Q. Fu, Z.F. Zhou, Structural and tribological properties of CrMoCN coatings with various Mo contents in artificial seawater, Appl. Surf. Sci. 493 (2019) 485–496.
- [39] E.C. Hornus, M.A. Rodríguez, R.M. Carranza, R.B. Rebak, Crevice corrosion repassivation of Ni-Cr-Mo alloys by cooling, Corrosion 75 (6) (2019) 604–615.
- [40] S.W. Watson, F.J. Friedersdorf, B.W. Madsen, S.D. Cramer, Methods of measuring wear-corrosion synergism, Wear 181 (1995) 476–484.
- [41] M.T. Mathew, T. Uth, N.J. Hallab, R. Pourzal, A. Fischer, M.A. Wimmer, Construction of a tribocorrosion test apparatus for the hip joint: validation, test methodology and analysis, Wear 271 (2011) 2651–2659.